NJC

This article can be cited before page numbers have been issued, to do this please use: D. Wang, H. Shen, G. Li, F. Fu and Y. Liang, *New J. Chem.*, 2016, DOI: 10.1039/C6NJ01893A.

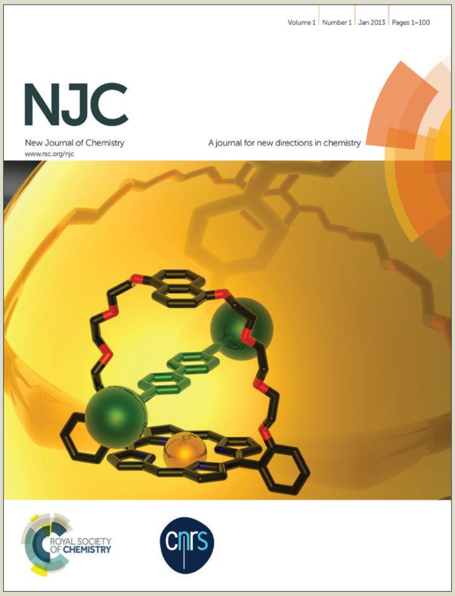

ROYAL SOCIETY OF CHEMISTRY

www.rsc.org/njc

View Article Online
DOI: 10.1039/C6NJ01893A

New Journal of Chemistry

ARTICLE

Received 00th January 20xx,
Accepted 00th January 20xx

DOI: 10.1039/x0xx00000x

www.rsc.org/

Design and Construction of the Sandwich-Like Z-scheme Multicomponent CdS/Ag/Bi_2MoO_6 Heterostructure with Enhanced Photocatalytic Performance in RhB Photodegradation

Danjun Wang,[a] Huidong Shen,[a] Li Guo,[a] Feng Fu*[a] and Yucang Liang*[b]

A sandwich-like Z-scheme tricomponent CdS/Ag/Bi_2MoO_6 photocatalytic system was rationally designed and successfully fabricated, in which Ag was loaded onto Bi_2MoO_6 microspheres by a facile photoreduction method and CdS was subsequently deposited onto the surface of Bi_2MoO_6 and Ag/Bi_2MoO_6 through a deposition-precipitation method. During this process, a series of Ag/Bi_2MoO_6 and CdS/Bi_2MoO_6 were also prepared. All composites were characterized by XRD, TEM, SEM, EDX, XPS, UV-vis DRS, and IR spectra to confirm the successful integration of Ag or (and) CdS with Bi_2MoO_6 and the alteration of morphology and the formation of new phase before and after Ag or (and) CdS loading. The degradation of Rhodamine B (RhB) dye under visible light irradiation (> 420 nm) revealed that CdS/Ag/Bi_2MoO_6 composite exhibited a highly visible-light-responsive photocatalytic performance compared to single Bi_2MoO_6 or CdS and dual Ag/Bi_2MoO_6 or CdS/Bi_2MoO_6. The enhanced photocatalytic performance of the CdS/Ag/Bi_2MoO_6 was ascribed to its special structure — a typical Z-scheme photocatalytic system, in which Ag nanoparticles directly connected to the surface of CdS and Bi_2MoO_6 to form the solid-solid interface (Ohmic contact) acting as a conductor that greatly shortened the distance of photogenerated electron transfer and performed the combination of photogenerated electrons from the CB of Bi_2MoO_6 with the photogenerated holes from the VB of CdS through the Ohmic contact, and thereby led to the efficient separation of photogenerated electrons and holes and showed stable and strong reducibility and oxidizability. Moreover, the surface plasmon resonance effect of metallic Ag nanoparticles also played an important role for the enhanced photocatalytic performance of RhB degradation under visible light irradiation. Furthermore, the investigations on photoluminescence and photoelectrochemical property also demonstrated indirectly the highly efficient separation of photogenerated electrons and holes in the Z-scheme CdS/Ag/Bi_2MoO_6 photocatalytic system. This new member of Z-scheme photocatalytic system will be applied to more photoreactions in further exploration.

1 Introduction

Semiconductor-based photocatalysis has been attracted considerable attentions due to a promising pathway for solving the increasingly serious energy and environmental problems.[1] In these photocatalytic performances, TiO_2 is a typical photocatalyst that is widely used in H_2 or O_2 production and the degradation of organic pollutants.[2-4] Unfortunately, TiO_2 as photocatalyst shows two main drawbacks: (i) A wide band gap of 3.2 eV, which can be photoactivated under UV light to exhibit low solar energy conversion efficiency;[5-7] (ii) The high recombination of photogenerated electron-hole pairs in the TiO_2 system leads to low quantum efficiency.[8] These shortcomings greatly limit its practical applications. Therefore, the development of highly efficient, sustainable and visible-light-responsive photocatalytic materials is urgent and indispensable.

Bismuth molybdate (Bi_2MoO_6) featured layered configuration is a simplest member of the Aurivillius family of layered perovskites, which consists of $[Bi_2O_2]^{2+}$ layers interleaved with perovskite-like $[MoO_4]^{2-}$ layers[9,10] and displays an excellent photocatalytic performance for completely degrading organic pollutants in waste water under visible light irradiation.[10-13] Bi_2MoO_6 as a semiconductor has a smaller band gap ranging from 2.5 to 2.8 eV and is capable of capturing visible light.[14] Owing to the low visible light utilization efficiency and the high recombination of photo-induced electrons and holes, the practical application of individual phase Bi_2MoO_6 was limited.[13,15,16] To overcome the intrinsic limitations of the

---

[a] *College of Chemistry &Chemical Engineering, Yan'an University, Shaanxi Key Laboratory of Chemical Reaction Engineering, Yan'an 716000, China. E-mail: yadxfufeng@126.com; +86-911-2332037.*
[b] *Institut für Anorganische Chemie, Eberhard Karls Universität Tübingen, Auf der Morgenstelle 18, 72076 Tübingen, Germany. E-mail:yucang.liang@uni-tuebingen.de;+49-7071-2976216.*

Electronic Supplementary Information (ESI) available: XRD patterns, UV-vis DRS spectra and comparison of the photocatalytic activity. See DOI: 10.1039/x 0xx00000x

View Article Online
DOI: 10.1039/C6NJ01893A

single-component Bi_2MoO_6, the heterojuncted or multi-component Bi_2MoO_6-based photocatalysts have been prepared to improve/enhance their property in repressing the recombination of photogenerated electron-hole pairs through an efficient charge transfer process and thereby drive efficient photo-reduction and oxidation reactions at spatially separated sites.[14,17-20] Hence the integration of heterocomposite into single-component Bi_2MoO_6 to prepare Bi_2MoO_6-based multi-composites is becoming a pivotal strategy for improving their photocatalytic performance in practical applications. CdS is an important II-VI semiconductive metal chalcogenide material regarded as a very promising class of visible-light-driven photocatalyst due to its wide light response (up to 520 nm or even longer).[21-23] But, the applications of pure CdS is encountering a enormous challenge — easy aggregation of small-sized single CdS particles and its instability in air[24,25] due to easy oxidation of S^{2-} in CdS. Note that CdS attached on the surface of the (non)metal-based composite fabricated heterojunction nanocomposites ($CdS@g\text{-}C_3N_4$ and CdS/Bi_2MoO_6), efficiently showing an enhanced visible light photocatalytic activity and photostability compared to pure CdS.[26-28] The improvement of the photocatalytic efficiency of photocatalysts is performed by promoting the fast effective separation of photogenerated electrons and holes (impeding the recombination of electron and hole as much as possible). In fact, photocatalysis is a light-driven chemical process over the surface of a photocatalyst[29] or is the acceleration of a photoinduced chemical reaction in the presence of catalyst, and photoinduction reaction is activated by absorption of a photon with sufficient energy[30] — water can produce hydrogen,[31-33] solar energy can convert into electric energy,[34,35] CO_2 can be reduced to organic fuels[36-38] and organic pollutants can be degraded.[39-41] The absorption leads to a charge separation — the formation of negative electron in the conduction band and of positive hole in valence band of the semiconductor catalyst. It is known that the electrons in less negative conduction band (CB) and holes in less positive valence band (VB) show weak redox ability.[20] Consequently, the typical semiconductor heterojunction displays a fatal shortcoming — the reduced redox ability of transferred electrons and holes, which negatively affect the photocatalytic reactions.[42] Thus, it is an enormous challenge to establish a photocatalytic system with both fast electron-hole separation and strong redox ability. Hence, the single-component photocatalyst is very difficult to simultaneously satisfy all strict requirements — ‘‘a wide absorption range, long-term stability, high charge-separation efficiency and strong redox ability’’, the multicomposite photocatalytic systems are becoming more and more important, especially, the all-solid-state Z-scheme photocatalytic systems. In 2006, an all-solid-state photosystem-conductor-photosystem (PS-C-PS) system — a so-called Z-scheme $CdS\text{-}Au\text{-}TiO_2$ system was reported for the first time, in which PSI(CdS), PSII(TiO_2) and the electron-transfer system (Au) were spatially fixed.[43] After that the artificial heterogeneous all-solid-state Z-scheme photocatalytic system has been widely investigated.[29] Especially note that the photogenerated electrons and holes are respectively left in the CB of photosystem I and the VB of photosystem II, and thereby carried out the efficient separation of electrons and holes. This process markedly differs from the conductor heterojunction-type charge transfer mechanism. Such a Z-scheme pathway of electron transfer can preserve the oxidative holes in the lower VB and reductive electrons in the higher CB, resulting in not only the great improvement of separation efficiency but also the strong reducibility of photogenerated electrons from photosystem I and the strong oxidizability of holes from photosystem II.[20,29] Up to present, several Z-scheme photocatalytic systems containing silver have been successfully designed and constructed for photocatalytic convert of solar energy and photocatalytic degradation of pollutants in waste water.[20,29,44-56]

Nevertheless, in a semiconductor heterojunction, the Z-scheme charge transfer process usually faces the competition of the typical charge transfer process.[29] A conductor or a contact interface with low contact resistance can be applied as an electron mediator to speed up the desirable specific carrier transfer.[43,45,52,56-58] For example, Ag has an excellent electron conductivity and has been often used as a mediator in many Z-scheme systems.[20,45-56] Moreover, Ag nanoparticles with localized surface plasmon resonance (SPR) properties have a strong absorption under visible light.[59,60] On the basis of these advantages, Ag particles as conductor have attracted considerable attention.[20,45,47-57,61]

In this paper, we rationally designed and successfully fabricated an all-solid-state Z-scheme $CdS\text{-}Ag\text{-}Bi_2MoO_6$ photocatalytic system including CdS and Bi_2MoO_6 as the visible-light active photocatalysts and Ag as a solid electron mediator, and showed an enhanced photocatalytic performance for degrading organic pollutants compared with single-component Bi_2MoO_6, dual Ag/Bi_2MoO_6 and CdS/Bi_2MoO_6. The enhanced performance of the $CdS/Ag/Bi_2MoO_6$ was ascribed to the separation efficiency of photoinduced carriers and the strong reducibility and oxidizability of the photogenerated electrons and holes. A Z-scheme charge transfer mechanism for efficiently separation of photogenerated electrons and holes was suggested to elucidate photocatalytic reactions over $CdS/Ag/Bi_2MoO_6$ photocatalyst by photoluminescence (PL) spectra, photocurrent generation and electrochemical impedance spectroscopy (EIS). Hence the combination of all advantage of the visible-light-responsive Ag, Bi_2MoO_6 and CdS photocatalysts in $CdS\text{-}Ag\text{-}Bi_2MoO_6$ system might be a promising strategy for improving highly efficient separation of electrons and holes and performing quick photodegradation of organic pollutants such as rhodamine B and methyl orange.

2 Experimental

2.1 Sample preparation

2.1.1 Preparation of Bi_2MoO_6

All the chemicals were analytical grade and used as received. Distilled water was used in all experiments. Bi_2MoO_6 microspheres were prepared according to slightly modified literature procedures.[19] In a typical process, a certain stoichiometric of $Bi(NO_3)_3 \cdot 5H_2O$ was dissolved in 13.0 mL of

View Article Online
DOI: 10.1039/C6NJ01893A

ethylene glycol (EG) under vigorous stirring, and 0.65 mmol of $Na_2MoO_4{\cdot}2H_2O$ powder was then added and continuously stirred for 30 min until a transparent solution was formed. Afterwards, 32.5 mL of ethanol was added and the mixture was stirred for another 30 min. Finally, the miscible solution was transferred into a 65.0 mL Teflon-lined stainless steel autoclave. The autoclave was sealed and maintained at 160 °C for 12 h, and then naturally cooled down to room temperature. The resulting precipitates were separated by centrifugation and washed with deionized water for several times and then dried at 60 °C for 12 h in a vacuum oven.

2.1.2 Synthesis of Ag/Bi_2MoO_6 photocatalysts

Silver nanoparticles deposited on the surface of Bi_2MoO_6 was prepared by a photoreduction process according to our previous work.[62] To a aqueous suspension of Bi_2MoO_6 (1.0 mmol), an appropriate amounts of $AgNO_3$ solution (18 mL, 10^{-4} $g{\cdot}mL^{-1}$) were added under stirring. Then the suspension was irradiated at ambient temperature for 3 h using a 400W xenon lamp under stirring. During the irradiation, the supernatant was collected and tested until Ag^+ was precipitated completely. After completed photoreduction process, the Ag-loaded Bi_2MoO_6 were filtered and washed with water to completely remove NO_3^- ions, and dried at 60 °C for 12 h in a vacuum oven. The theoretically deposited amount of Ag is 1.0 at% to Bi_2MoO_6, and the resulted sample Ag/Bi_2MoO_6 was noted as A/BMO.

2.1.3 Fabrication of $CdS/Ag/Bi_2MoO_6$ photocatalyst

All the $CdS/Ag/Bi_2MoO_6$ photocatalyst were fabricated via a deposition-precipitation method. A detail procedure is as follows: the obtained Ag/Bi_2MoO_6 (0.6099 g) was dispersed in 25 mL of absolute ethanol solution for 1 h under stirring, and an appropriate amounts of $Cd(CH_3COO)_2{\cdot}2H_2O$ were then added. After being stirred at ambient temperature for 2 h, equimolar thioacetamide (TAA) ethanol solution (0.133 M) was added to the above suspension and stirred at room temperature for another 1 h. The suspension was sealed in a Teflon-lined stainless steel vessel and heated at 180 °C for 10 h. After cooled down to room temperature, the as-prepared product was centrifugally separated and washed with water and absolute ethanol for several times. Finally, the as-made sample was dried at 60 °C in a vacuum oven to obtain $CdS/Ag/Bi_2MoO_6$ (C/A/BMO). The $CdS/Ag/Bi_2MoO_6$ composites with molar ratio of CdS to Ag/Bi_2MoO_6 of 80, 100, 120, 140 and 160 % were marked as 80 at% C/A/BMO, 100 at% C/A/BMO, 120 at% C/A/BMO, 140 at% C/A/BMO and 160 at% C/A/BMO, respectively. The same procedure was used to prepare 120 at% CdS/Bi_2MoO_6 by depositing CdS on the surface of pure Bi_2MoO_6, and the obtained product was marked as 120 at% C/BMO. For comparison, single CdS was prepared via a similar procedure in the absence of Bi_2MoO_6.

2.2 Characterization

Powder X-ray diffraction (XRD) was carried out on a Shimadzu XRD-7000 X-ray diffractometer using Cu Kα radiation (λ = 0.15418 nm) at a scanning rate of 2° min^{-1} in a 2θ range of 5° - 80°. The accelerating voltage and the applied current were 40 kV and 30 mA, respectively. X-ray photoelectron spectroscopy (XPS) was recorded on a PHI-5400 X-ray photoelectron spectrometer. Field emission scanning electron microscope (FE-SEM) images were recorded on a JSM-6700F scanning electron microscope. High-resolution transmission electron microscope (HRTEM) images and selected area electron diffraction (SAED) patterns were recorded on a JEM-2100 electron microscope operated at an accelerating voltage of 200 kV. The UV-Vis diffuse reflectance spectra (UV-Vis-DRS) of the samples were obtained using Shimadzu UV-2550 UV-Vis spectrophotometer. $BaSO_4$ was used as a reflectance standard. Photoluminescence (PL) spectra were measured using a F-4500 spectrophotometer (Hitachi, Japan) at an excitation at 400 nm.

2.3 Photocurrent-time measurement

Photocurrent measurements were performed on an electrochemical analyzer (CHI660D, CHI Shanghai, Inc.) in a standard three-electrode configuration with a platinum wire as a counter electrode and a saturated calomel electrode (in saturated KCl) as a reference electrode. A 400W xenon lamp with an UV cutoff filter (λ > 420 nm) is employed as the light source. Na_2SO_4 (0.1 M) aqueous solution was used as the electrolyte. The typical working electrode was prepared as follows: the 10 mg ground sample was dispersed ultrasonically in 2 mL of distilled water to make a slurry. The slurry was then dispersed onto an ITO glass electrode with an active area of about 1.0 cm^2, and the electrode was dried at 60 °C for 6 h. Electrochemical impedance spectra (EIS) were measured.

2.4 Photocatalytic activity

The evaluation of the photocatalytic performance of samples for photocatalytic decolorization of RhB aqueous solution was performed as follows: A 400W halogen lamp was used as the visible-light source with a cutoff filter to cut off the light below 420 nm. The suspension containing 200 mg of photocatalyst and 200 mL of fresh aqueous solution of RhB (10 mg L^{-1}) were continuously stirred in the dark for 1.0 h to establish an adsorption/desorption equilibrium of RhB solution. After this period of time, the light source was turned on. During the reaction, 5.0 mL of samples were taken at given time intervals and the photocatalysts (Bi_2MoO_6) were then separated by centrifugation. The supernatant solution was decanted and the absorbance of RhB was determined through its maximum absorption band using a Shimadzu 2550 UV-visible spectrophotometer and the absorption peak at 553 nm was monitored to obtain the photocatalytic degradation efficiency.[63]

3 Results and discussion

3.1 Determination of Z-scheme $CdS/Ag/Bi_2MoO_6$ using XRD analysis

Fig. 1 shows XRD patterns of single-component Bi_2MoO_6 and CdS, dual CdS/Bi_2MoO_6 (120 at% C/BMO) and Ag/Bi_2MoO_6, and tri-component $CdS/Ag/Bi_2MoO_6$ (120 at% C/A/BMO). All the diffraction peaks can be attributed to single composite Bi_2MoO_6 (JCPDS card No.76-2388), Ag (JCPDS card No.04-

View Article Online
DOI: 10.1039/C6NJ01893A

0783) and CdS (JCPDS card No. 89-0440), respectively. For samples A/BMO, C/BMO and C/A/BMO, the characteristic diffraction peaks of BMO still preserve. However the XRD pattern of sample Ag/Bi_2MoO_6 indicates two weak well-resolved diffraction peaks at 2θ = 38.12° and 44.28°, which are indexed as the (111) and (200) reflection planes of face-centered cubic Ag particles with *Fm-3m* space group (marked with the triangle ▼). For C/BMO heterostructure, the diffraction peaks corresponded to CdS phase (JCPDS card No. 89-0440) are observed, confirming the deposition of CdS phase on BMO. For C/A/BMO composite, after deposited CdS on the surface of A/BMO, some new diffraction peaks appear at 2θ angle of 26.46°, 43.89° and 51.98°, which can be indexed as (111), (220) and (311) reflection planes of face-centered cubic CdS crystalline particles with *F-43d* symmetry. The XRD patterns of other Z-scheme C/A/BMO (80 at%, 100 at%, 140 at%, 160 at%) are similar to that of 120 at% C/A/BMO (Fig. S1). Owing to the overlap of diffraction peaks of Ag and CdS phases, the positions of diffraction peaks are slightly shifted compared to a single Ag and CdS composite. These results based on XRD analysis clearly corroborate that Z-scheme C/A/BMO composites were successfully synthesized.

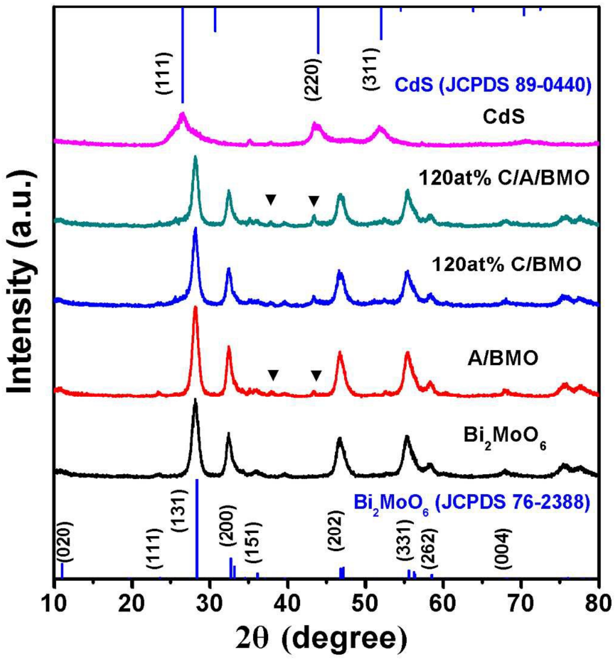

Fig. 1 XRD patterns of pure Bi_2MoO_6 and CdS, dual A/BMO and 120 at% C/BMO, ternary 120 at% C/A/BMO composites.

3.2 Morphology and microstructure of Z-scheme C/A/BMO composite by FE-SEM and TEM analysis

The morphology and microstructure of the pure Bi_2MoO_6 and CdS, dual A/BMO and as-prepared C/A/BMO composites are directly investigated by SEM and (HR)TEM. The Bi_2MoO_6 microspheres with average diameter of 1 - 2 μm are composed of a large amount of nanoplates with the thickness of 20 - 50 nm (Fig. 2a, 2b). The as-made CdS consists of nanospheres without uniform size, and these small nanospheres are aggregated together to form bulk clusters (Fig. S2a). Compared with the pure Bi_2MoO_6, the morphology of Ag/Bi_2MoO_6 composite is quite similar to that of precursor Bi_2MoO_6 in a large area (Fig. 2c, 2d), but some small spherical Ag particles loaded onto the surface of the Bi_2MoO_6 architectures are observed anywhere, indicating that Ag nanoparticles were successfully prepared and highly dispersed on the surface of the Bi_2MoO_6 nanoarchitectures, which is well consistent with the XRD results. For the as-made C/A/BMO composite, the SEM images clearly indicate that many irregularly spherical CdS particles deposited on the surface of A/BMO performed the partial or complete coverage of A/BMO, showing the formation of obvious agglomerations (Fig. 2e, 2f). To further identify the presence of CdS and Ag on the surface of Bi_2MoO_6 microspheres, the microanalysis of the C/A/BMO composite was examined by the energy dispersive X-ray (EDX) spectroscopy. The EDX spectrum came from Fig. 2f is shown in Fig. 2g, confirming that the composite contained elements Ag, Bi, Mo, O, Cd and S.

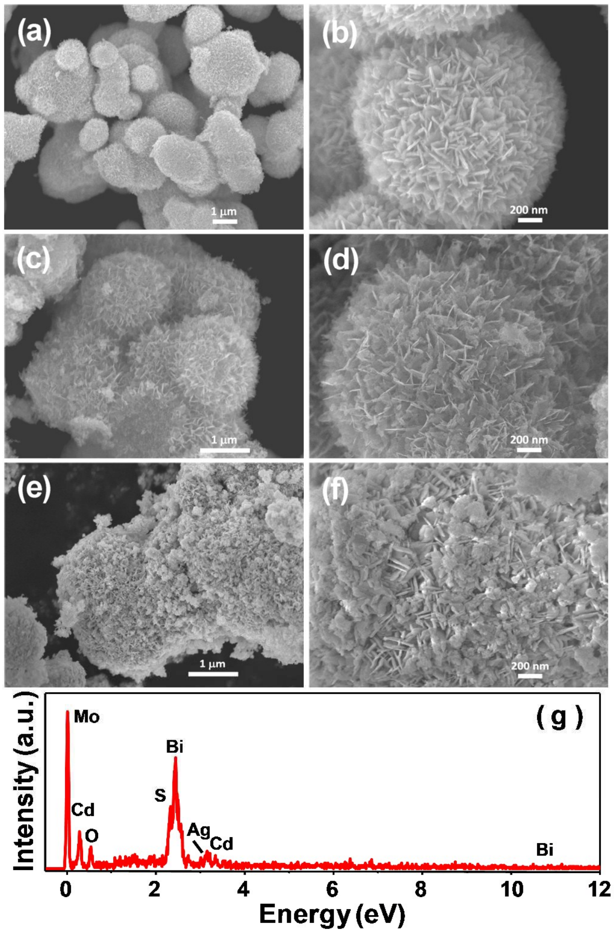

Fig. 2 FE-SEM images of (a, b) as-prepared pure Bi_2MoO_6, (c, d) A/BMO, (e, f) 120 at% C/A/BMO composites, and (g) EDX profile of 120 at% C/A/BMO.

To further identify the microstructure of the as-synthesized C/A/BMO composite, transmission electron microscopy (TEM) was performed and the representative TEM images are shown

View Article Online
DOI: 10.1039/C6NJ01893A

in Fig. 3. For the pure Bi_2MoO_6, a flower-like microsphere structure is observed (Fig. 3a). Single-component CdS is composed of irregular nanoparticles with the size of about 10 nm (Fig. S2b). For Z-scheme photocatalytic system C/A/BMO the representative (HR)TEM images are presented in Fig. 3b and 3c. The measured lattice fringes of the (131) plane of Bi_2MoO_6 with *d*-spacing of 0.317 nm, of the (200) plane of Ag with *d*-spacing of 0.204 nm, and of the (111) plane of CdS with *d*-spacing of 0.337 nm, are in better agreement with that from the wide angle PXRD data, further demonstrating the presence of face-centered cubic Ag and CdS phases in Bi_2MoO_6 composite. Moreover, for 120 at% C/A/BMO nanocomposite, the high-angle annular dark field scanning transmission electron microscopy (HAADF-STEM) image in Fig. 3d and the spatial distribution of the element composition along the edge of the particles in Fig. 3e investigated by line-scanning elemental mappings, clearly corroborated a well-defined composition profile of C/A/BMO nanostructures. The profiles of Bi, Mo and O show a narrow band-like peak at the center, whereas the profiles of Ag, S and Cd show slightly sharp peaks at the right and left sides with a broad valley at the center, showing a clear interface between CdS and Bi_2MoO_6 components of the heterostructures.

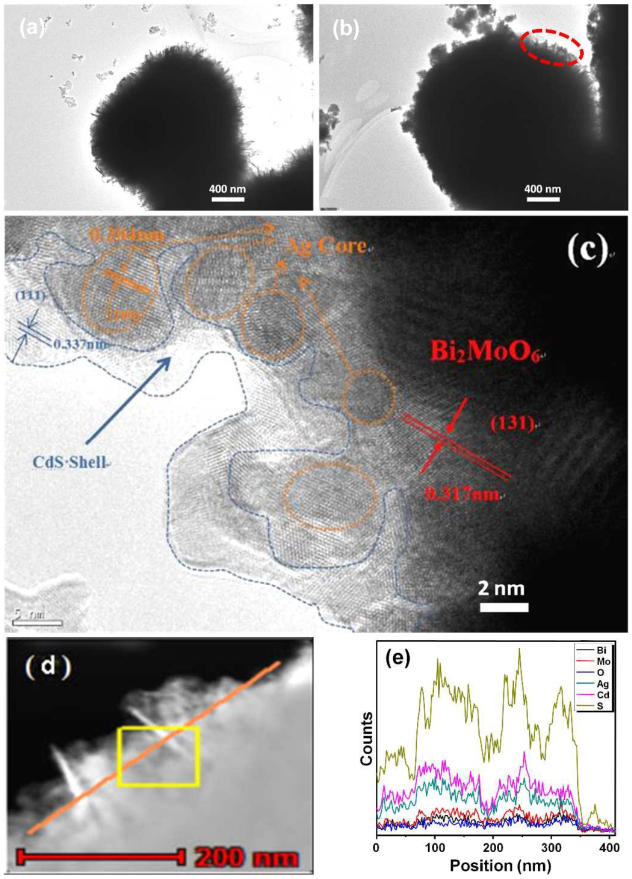

Fig. 3 TEM image of (a) Bi_2MoO_6, (b) C/A/BMO, (c) HRTEM image of C/A/BMO, (d) HAADF-STEM image of C/A/BMO composite, and (e) EDX line-scanning elemental mappings of a single C/A/BMO particle (indicated by red line in (b)).

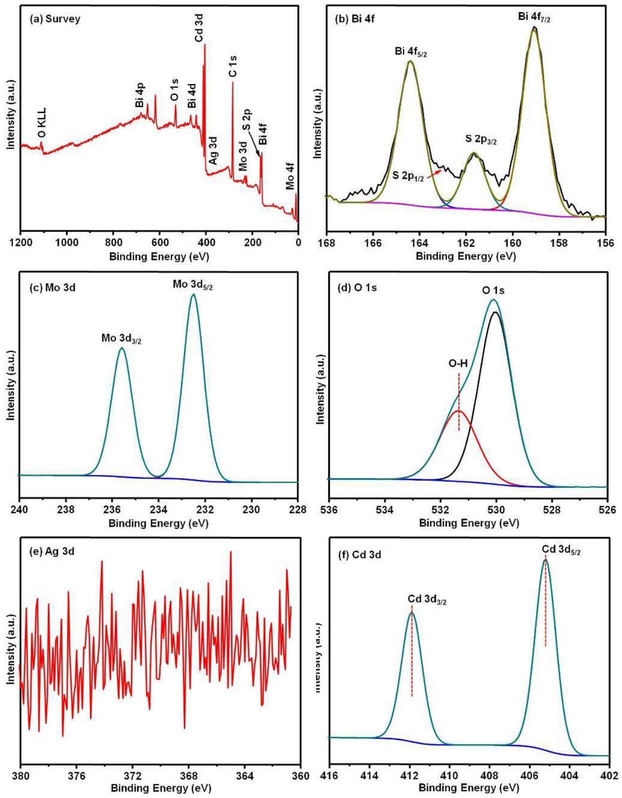

Fig. 4 XPS spectra of sample 120 at% C/A/BMO: (a) The survey spectrum, (b) Bi 4f and S 2p, (c) Mo 3d, (d) O 1s, (e) Ag 3d, and (f) Cd 3d.

3.3 XPS analysis

XPS spectra of the samples are performed to investigate the surface valence state and the chemical composition. As shown in Fig. 4a, the XPS survey spectra are mainly composed of Bi, Mo, O, Ag, S and Cd elements, which are consistent with the chemical composition of the photocatalysts. The C element came from the adventitious hydrocarbon of the XPS instrument itself. The high resolution spectra of Bi 4f, Mo 3d, O 1s, Ag 3d, and Cd 3d of sample 120 at% C/A/BMO are shown in Fig. 4b-f, respectively. As viewed in Fig. 4b, two strong peaks at around 158.5 and 163.7 eV are observed, which can be assigned to the binding energy of Bi $4f_{7/2}$ and Bi $4f_{5/2}$, respectively.[64] Two bands at 232.2 and 235.3 eV in Fig. 4c are ascribed to Mo $3d_{5/2}$ and Mo $3d_{3/2}$, respectively.[65] The observed two O 1s peaks at 531.2 and 529.9 eV in Fig. 4d are in agreement with OH hydroxyl groups and oxygen species in the lattice oxygen, respectively.[66] Moreover, the Ag 3d spectrum monitored is very weak due to a very low loading of Ag (Fig. 4e). However, the XPS spectrum of Cd 3d clearly indicates two characteristic bands at 404.9 and 412.3 eV, which can be assigned to the Cd^{2+} ions in CdS.[67] Furthermore, the S element can also be detected by XPS spectrum in Fig. 4b at around 160.5 and 159.5 eV, revealing binding energy of characteristic S $2p_{3/2}$ and S $2p_{1/2}$, respectively.[68,69] As comparison, the high-resolution XPS spectra of Cd 3d of pristine CdS, Bi 4f of pristine Bi_2MoO_6 and 120 at% C/A/BMO are shown in Fig. S3. The binding energy of Bi $4f_{5/2}$ and Bi $4f_{7/2}$ of Bi_2MoO_6 is lower (0.2 eV) than those

View Article Online
DOI: 10.1039/C6NJ01893A

of the 120 at% C/A/BMO (Fig. S3a). Note that the binding energy of the Cd $3d_{3/2}$ and Cd $3d_{5/2}$ from pure CdS is higher (0.25 eV) than those from the 120 at % C/A/BMO (Fig. S3b). These results imply that the deposited CdS nanoparticles are probably attached on the surface of BMO, not *via* a simply physical mixture.[70] Based on these XPS results, Ag and CdS have been successfully loaded on the surface of Bi_2MoO_6 to fabricate a Z-scheme C/A/BMO photocatalytic system which has been confirmed by the HRTEM and EDX measurement.

3.4 FT-IR spectra analysis

To investigate the chemical composition and characteristic chemistry bonding of the composites, the Fourier transform infrared spectroscopy (FT-IR) was carried out. Fig. 5a shows the FT-IR spectra of the as-prepared pure Bi_2MoO_6, A/BMO, 120 at% C/BMO, 120 at% C/A/BMO and pure CdS. For pure Bi_2MoO_6, the characteristic Mo-O asymmetric and symmetric stretching vibrations of MoO_6 octahedron involving vibration of the apical oxygen atoms appear at 843 and 797 cm^{-1}, respectively.[71-73] Moreover, the bands, at 734 cm^{-1} attributed to the Mo-O asymmetric stretching mode involving vibrations of the equatorial oxygen atoms from MoO_6, and at 603 and 570 cm^{-1} assigned to the bending vibration of MoO_6, as well as at 455 cm^{-1} belonged to the Bi-O stretching and bending vibrations from BiO_6 unit, are observed as previous study reported by Zhu and co-workers.[73] For single-component CdS, the characteristic Cd-S bond appears at 1384 and 1118 cm^{-1}.[74] Owing to surface adsorption of water on CdS, the O-H bending vibration appears at 1630 cm^{-1}.[26] It is worth noting that a absorption peak appears at about 1045 cm^{-1} for A/BMO and 120 at% C/A/BMO, which can be attributed to the resonance absorption of Ag nanoparticles. For samples Ag/Bi_2MoO_6, C/BMO and C/A/BMO, the correspondingly characteristic chemistry bonding vibrations (Mo-O, Cd-S and Bi-O) appear in their IR spectra, clearly verifying the successful synthesis of corresponding composites. These results are in good agreement with data from the XRD, SEM and (HR)TEM analysis.

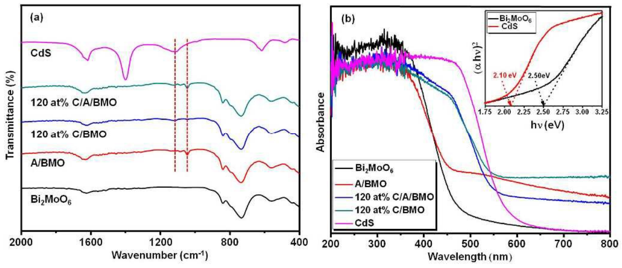

Fig. 5 (a) FT-IR spectra and (b) UV-vis DRS spectra of pure Bi_2MoO_6 and CdS, dual A/BMO and 120 at% C/BMO, and Z-scheme ternary 120 at% C/A/BMO composites. The inset is the plot of absorption $(\alpha h\nu)^2$ versus energy (hν) for the band gap energy of pure Bi_2MoO_6 and CdS.

3.4 UV-vis-DRS analysis

The typical UV-vis diffuse reflectance spectroscopy (UV-vis-DRS) is a useful method to reflect the optical absorption properties of the as-prepared samples. As viewed in Fig. 5b and Fig. S4, the absorption edge of pure Bi_2MoO_6 is estimated to be 470 nm, while pure CdS shows a strong absorption at 556 nm in the UV range. The multicomposites A/BMO, 120 at% C/BMO, and 120 at% C/A/BMO and other Z-scheme C/A/BMO (80 at%, 100 at%, 140 at%, 160 at%) respectively exhibit a strong absorption ability in the range of 400-800 nm compared to pure Bi_2MoO_6, indicating that the loading of Ag and CdS can effectively enhance the visible-light absorption. For A/BMO, it is noteworthy that an extra absorption peak at the visible-light absorption region (about 540 nm) is found and can be ascribed to the surface plasmon resonance (SPR) absorption of the Ag nanoparticles.[59,60] However, for C/A/BMO composite, the SPR absorption significantly broadens and occurs a red-shift of the Ag surface plasmon band of about 100 nm compared with A/BMO, suggesting a strong electronic interaction between Ag and CdS.[43,75] Therefore, this phenomenon corroborates that the Ag nanoparticles deposited on Bi_2MoO_6 are coated by CdS.

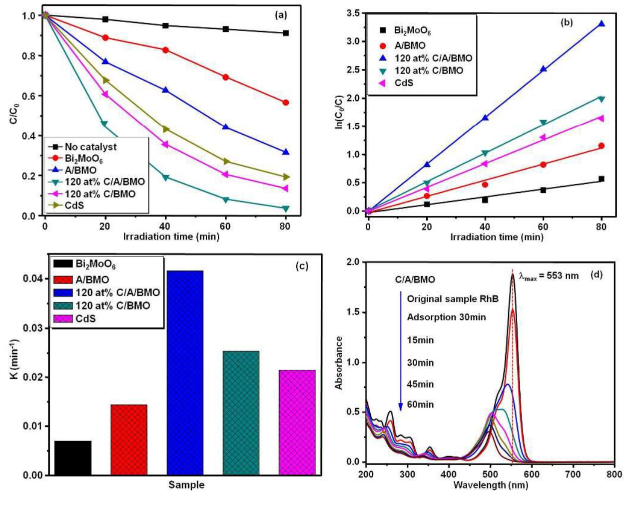

Fig.6 (a) Photocatalytic degradation efficiency of RhB by pure Bi_2MoO_6, A/BMO, 120 at% C/BMO, 120 at% C/A/BMO composites and single CdS; (b) kinetic plot of C/C_0 versus irradiation time for the photodegradation of RhB with different photocatalysts, (c) Rate constants of the photodegradation of RhB using different photocatalysts, and (d) The change of the absorption spectra of photodegradated RhB with increasing irradiation time under visible light using 120 at% C/A/BMO composite as a photocatalyst.

The band gap energy (E_g) of the semiconductors are calculated from a plot of $(\alpha h\nu)^{2/n}$ versus energy (hν) (Fig. 5b, inset) according to the equation of the optical absorption near band edge: $\alpha h\nu = A(h\nu - Eg)^{n/2}$,[76] where α, *hν*, E_g and A are the optical absorption coefficient, photonic energy, photonic energy band gap, and proportionality constant, respectively. In this equation, *n* depends on whether the transition is direct (n = 1) or indirect (n = 4). As shown in the literature, Bi_2MoO_6 and CdS is an direct optical transition type semiconductor.[77,78] The direct band gaps of pure Bi_2MoO_6 and CdS can be obtained from the chart of absorption $(\alpha h\nu)^2$ versus energy hν (Fig. 5b, inset). Thus, the band gaps of pure Bi_2MoO_6 and CdS are determined to be 2.10 and 2.50 eV, respectively.

3.5 Photocatalytic activity

Photocatalytic decomposition of RhB on various samples as photocatalysts is evaluated under visible light irradiation ($\lambda >$ 420 nm). Fig. 6a presents the photocatalytic degradation results

View Article Online
DOI: 10.1039/C6NJ01893A

of RhB over single component CdS, pure Bi_2MoO_6, A/BMO, 120 at% C/BMO, and 120 at% C/A/BMO composites. The results indicate that the photocatalytic degradation efficiency of RhB was approximately 40% using pure Bi_2MoO_6 as a photocatalyst after irradiation for 80 min. Low yield is probably caused by the rapid recombination of photogenerated electrons and holes of the Bi_2MoO_6 microspheres. As compared to the pure Bi_2MoO_6, both A/BMO and C/BMO as catalysts significantly improve the photocatalytic activity, proving that Ag nanoparticles and CdS acted as an important role to enhance the photocatalytic performance. It is interesting to note that the 120 at% C/A/BMO as a photocatalyst displays the highest photocatalytic degradation efficiency compared to pure Bi_2MoO_6, A/BMO and C/BMO. Highly photocatalytic performance is attributed to the positive synergism of Ag and CdS on the surface of Bi_2MoO_6. Hence for the photodegradation of RhB the photocatalytic activity of all catalysts used is as follows in order from slow to fast: Bi_2MoO_6 < A/BMO < CdS < 120 at% C/BMO< 120 at% C/A/BMO. In addition, the screening of all the Z-scheme C/A/BMO photocatalysts with different amounts of CdS for the enhanced photocatalytic activities is shown in Fig. S5, clearly revealing that 120 at% C/A/BMO is a best photocatalyst. Furthermore, in order to better compare the photocatalytic efficiency of the all samples, the reaction kinetics of RhB degradation was investigated. According to the Langmuir-Hinshelwood (L-H) kinetics model,[79,80] the pseudo first-order kinetics equation is expressed as $\ln(C_0/C) = k_{app} \cdot t$, where k_{app} denotes the apparent rate constant (min^{-1}), C_0 and C are the RhB concentrations (mg L^{-1}) in solution at time $t = 0$ and $t = t$, t represents the irradiation time (min). With increasing irradiation time the plot of $\ln(C_0/C)$ versus irradiation time (t) for RhB degradation over different photocatalysts is shown in Fig. 6b. The results reveal that the photodegradation of RhB is a typical pseudo first-order reaction in the presence of photocatalysts (Bi_2MoO_6, A/BMO, C/BMO and C/A/BMO). The corresponding rate constants (k_{app}) of the photodegradation of RhB are shown in Fig. 6c, the corresponding rate constants k_{app} are 6.92×10^{-3}, 1.43×10^{-2}, 2.146×10^{-2}, 2.534×10^{-2} and 4.155×10^{-2} min^{-1} for pure Bi_2MoO_6, A/BMO, single-phase CdS, 120 at% C/BMO and 120 at% C/A/BMO, respectively. These findings clearly confirm that C/A/BMO composite is a highest active photocatalyst for the photocatalytic degradation of RhB, its activity is approximately 6 times higher than that of pure Bi_2MoO_6.

The temporal evolution of the absorption spectra of photodegraded RhB with increasing irradiation time are illustrated in Fig. 6d in the presence of catalyst 120 at% C/A/BMO composite. At the beginning of photodegradation, the strongest absorbance of RhB locates at 554 nm, and with increasing irradiation time the absorption peak gradually decreases and takes place a blue-shift until 498 nm after 80 min irradiation. The blue-shift is caused by the N-deethylation and deethylation of RhB during irradiation.[81]

3.6 Photoluminescence analysis

Owing to the photoluminescence (PL) emission originates from the recombination of free charge carriers, PL spectra is often used to investigate the efficiency of separation and transfer of photogenerated charge carrier and the fate of photogenerated electrons and holes in semiconductors.[69,71,82] It's well known that the lower PL intensity indicates less recombination rate of photogenerated electron-hole pairs and thereby shows high photocatalytic activity.[64] Hence we measured the PL emission spectra of pure Bi_2MoO_6, Ag/Bi_2MoO_6, C/BMO (120 at%), C/A/BMO (120 at%) composite and single CdS as shown in Fig. 7. For the pure Bi_2MoO_6, one characteristic emission peak centred at about 460 nm is observed, which is in accordance with previously reported results.[71,83] After introduced Ag nanoparticles and CdS onto the surface of Bi_2MoO_6, the intensity of the PL emission of C/A/BMO composites is obviously lower than that of other samples, implying that the incorporation of Ag and CdS nanoparticles on BMO composite can effectively repress the recombination of electron-hole pairs and thereby generate a higher photocatalytic activity, which is in good agreement with the result from RhB photodegradation experiment.

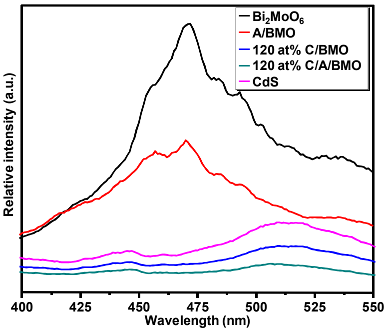

Fig. 7 PL spectra of pure Bi_2MoO_6 and CdS, A/BMO, 120 at% C/BMO and 120 at% C/A/BMO composite.

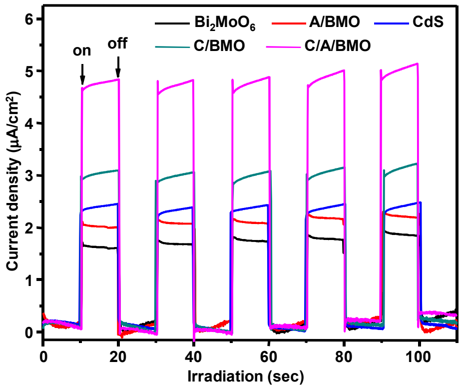

Fig. 8 Comparison of transient photocurrent responses of pure Bi_2MoO_6 and CdS, A/BMO, 120 at% C/BMO, and 120 at% C/A/BMO composite under visible light irradiation (λ > 420 nm, $[Na_2SO_4]$ = 0.1 M).

3.7 Photoelectrochemical property

The photocurrent measurements are usually utilized to investigate the interfacial charge transfer dynamics. A high photocurrent implies a high separation efficiency of electrons

View Article Online
DOI: 10.1039/C6NJ01893A

and holes, showing a high photocatalytic activity.[84] Fig. 8 displays the transient photocurrent responses of pure Bi_2MoO_6, 120 at% C/BMO, 120 at% C/A/BMO and single CdS with several on-off cycles of visible light illumination. In comparison with pure Bi_2MoO_6 and single CdS, C/A/BMO exhibits a significantly enhanced transient photocurrent density, which is about 3 times and 2 times higher than that of the pure Bi_2MoO_6 and single CdS, respectively. The results reveal that the C/A/BMO possesses the higher separation efficiency of photogenerated electrons and holes, further corroborating that the synergism of Ag and CdS on the surface of Bi_2MoO_6 is far superior to that of pure Bi_2MoO_6, CdS/Bi_2MoO_6 composite and single CdS.

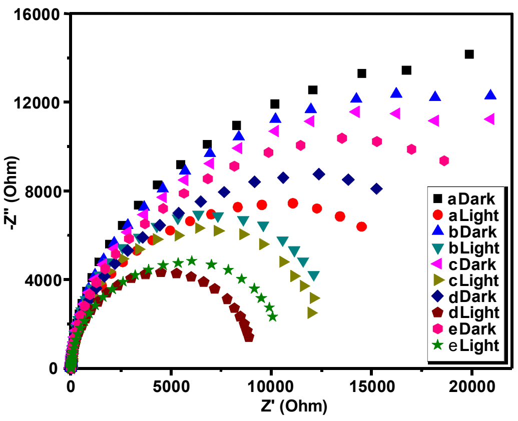

Fig. 9 Electrochemical impedance Nyquist plots of samples (a) pure Bi_2MoO_6, (b) A/BMO; (c) CdS, (d) 120 at% C/A/BMO, (e) 120 at% C/BMO electrodes under dark and light irradiation in the 0.5 M Na_2SO_4 electrolyte.

Moreover, the migration and transfer processes of photogenerated electrons and holes in a semiconductor can also be verified by the typical electrochemical impedance spectrum (EIS).[85] The radius of the arc in the EIS reflects the interface layer resistance occurred on the surface of electrode. The previous studies revealed that the smaller radius of the arc implied the higher efficiency of charge transfer.[86-88] As shown in Fig. 9, the typical EIS Nyquist plots of the pure Bi_2MoO_6, A/BMO, 120 at% C/BMO, 120 at% C/A/BMO and single CdS before and after visible light irradiation, clearly show that the arc radius of A/BMO and C/BMO is smaller than that of the pure Bi_2MoO_6 and CdS under light or dark conditions, but is bigger than that of C/A/BMO composite, implying that sample C/A/BMO (120 at%) possesses a stronger ability in separation and transfer of photogenerated electron-hole pairs. This result indicates that the incorporation of Ag and CdS on the surface of Bi_2MoO_6 can effectively enhance the separation and transfer of photogenerated electron-hole pairs and thereby leads to the improvement of photocatalytic degradation efficiency. The results of the EIS are in accordance with the aforementioned PL and photocurrent. Subsequently, the photocurrent generation and EIS experiments better demonstrate the electron excitation and the charge transport characteristics of 120 at% C/A/BMO samples.

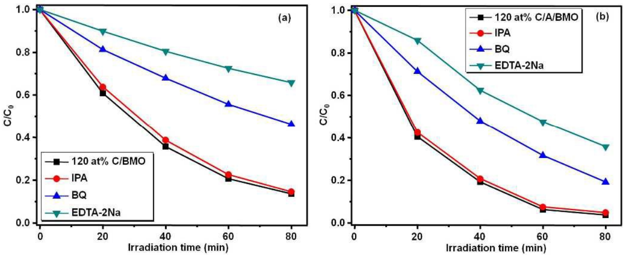

Fig. 10 Trapping experiments of active species for RhB photodegradation in the presence of photocatalyst (a) 120 at% C/BMO, (b) 120 at% C/A/BMO under visible light irradiation.

3.8 Photocatalytic mechanism

During the photodegradation process of organic pollutants, the active species including superoxide anion radicals ($\cdot O_2^-$), positive holes (h^+) and hydroxyl radicals ($\cdot OH$) are playing a crucial role. To further reveal the possible mechanism of the enhanced photocatalytic performance, the trapping experiment for identifying main active species was performed. The sacrificial agents, such as disodium ethylene diamine-tetraacetate (EDTA-2Na), isopropanol (IPA) and benzoquinone (BQ), are utilized as the scavengers of h^+, $\cdot OH$ and $\cdot O_2^-$, respectively.[89,90] The trapping experiments of active species upon the photocatalytic reactions of the samples shown in Fig. 10 indicates that IPA is almost not affect on photocatalytic efficiency, while the photocatalytic activity of the samples are obviously inhibited by the addition of the EDTA-2Na and BQ. This fact demonstrates that superoxide anion radicals $\cdot O_2^-$ and positive holes h^+ are mainly active species and are playing key roles in the RhB photodegradation process to compare with hydroxyl radical $\cdot OH$ in the presence of composites 120 at% C/BMO or 120 at% C/A/BMO under visible light irradiation. Nevertheless, the addition of EDTA-2Na quickly represses RhB degradation compared to that with the addition of BQ, revealing that positive holes h^+ play a more important role than hydroxyl radical $\cdot O_2^-$ in the photocatalytic reactions.

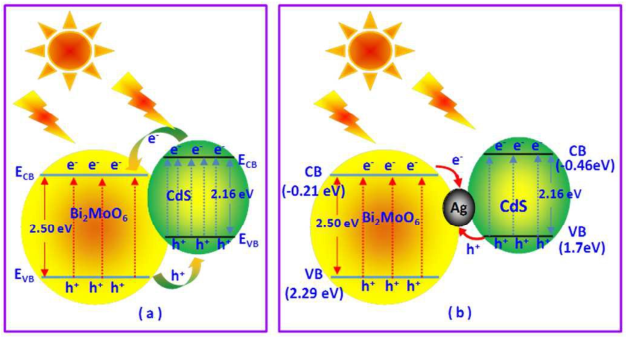

Fig. 11 Schematic illustration for the charge transfer in samples (a) C/BMO and (b) C/A/BMO under visible light irradiation.

To further confirm the formation of the Z-scheme C/A/BMO, the energy band levels of the Bi_2MoO_6 and CdS are determined. As shown in Fig. 11a, the band gaps of Bi_2MoO_6 and CdS are 2.5 and 2.16 eV, respectively. The calculated VB positions of Bi_2MoO_6 and CdS are approximately 2.29 and 1.7 eV,

View Article Online
DOI: 10.1039/C6NJ01893A

respectively, *via* the equation $E_{CB} = \chi - E^e - E_g$, and their corresponding CB edge levels (E_{CB} *vs* NHE) are calculated to be −0.21 and −0.46eV, respectively, *via* the equation $E_{VB} = E_g + E_{CB}$, where E_{CB} is the CB edge potential, E_{VB} is the VB edge potential, and χ is the electronegativity of the semiconductor. E^e is the energy of free electrons on the hydrogen scale ≈ 4.5 eV and E_g is the band gap of the semiconductor.[70,91] Based on the energy band levels of the Bi_2MoO_6 and CdS and the above-mentioned the trapping experiments of active species, herein, we suggest that the photogenerated charge migration in the C/BMO composite is similar to the typical charge migration mechanism of a semiconductor heterojunction (Fig. 11a). When the Bi_2MoO_6 and CdS are excited by visible light irradiation, the photogenerated electrons on the CB of CdS can easily migrate to the CB of Bi_2MoO_6, while the photogenerated holes in the VB of Bi_2MoO_6 can transfer to the VB of CdS. As a result, the photogenerated electrons and holes are spatially separated and greatly weakened undesirable recombination. But in the CdS-Bi_2MoO_6 system, due to that the top of the valence band potential of CdS is less positive than that of Bi_2MoO_6 and the bottom of conduction band potential of Bi_2MoO_6 is less negative than that of CdS, it is difficult to simultaneously possess the high charge-separation efficiency and strong redox ability, and thereby show a weak redox ability, especially after charge transfer. As shown in Fig. 11a, the holes density in the VB of Bi_2MoO_6 is depleted while holes density in the VB of CdS is enhanced during the photocatalytic process, hence, the redox ability of transferred electrons and holes are reduced,[42,92] showing a negative effect for the photocatalytic reactions. Note that the catalytic performance of this type of photocatalyst is much higher than that of single semiconductor and single-component catalyst. As a result, for the RhB photodegradation, the catalytic performance shown in Fig. 6a clearly reveals that the heterojunction-type C/BMO catalyst displays a higher photocatalytic behavior than single semiconductor CdS and single Bi_2MoO_6 due to the effective separation of the photogenerated electrons and holes. For C/A/BMO photocatalytic system, a different mechanism is suggested as shown in Fig. 11b. Although the spatial separation of photogenerated electrons and holes in Z-scheme C/A/BMO are similar to that from the heterojunction-type catalyst C/BMO under light irradiation, the photogenerated electrons from the CB of Bi_2MoO_6 can readily recombine with the photogenerated holes from the VB of CdS by Ohmic contact Ag NPs as conductor, because on the one hand, equilibrium of the Fermi levels has established at the solid-solid interfaces of Bi_2MoO_6, Ag and CdS before light irradiation. On the other hand, the strong SPR effect of Ag nanoparticles results in an enhanced local electric field around the solid-solid interfaces, which can drive the excited electrons of Ag to inject into the VB of CdS to recombine with holes or into the CB of CdS via direct electron transfer or plasmon-induced resonant energy transfer.[20,93] As a result, the photogenerated electrons in the VB of CdS continuously transit to the CB of CdS under light irradiation, and the photogenerated electrons aggregate in the CB of CdS to form an electron-rich region and thereby suppress the photo-oxidation of CdS, while the photogenerated holes aggregate in the VB of Bi_2MoO_6 to make a hole-rich region and therefore protect Bi_2MoO_6 from the photo-reduction. Hence the electron-rich region and the hole-rich region readily take place strong photo-reduction and photo-oxidation, respectively, indicating a high photocatalytic performance with a spontaneous and circular photo-reduction and photo-oxidation. Moreover the photogenerated electrons from the CB of Bi_2MoO_6 can directly recombine with the photogenerated holes from the VB of CdS through the Ohmic contact Ag nanoparticles, which greatly reduces the distance of Z-scheme electron transfer. This further improves efficient separation of electrons from CB of CdS and holes from the VB of Bi_2MoO_6. This is why Z-scheme catalyst C/A/BMO indicates a highest photocatalytic performance in RhB photodegradation compared to C/BMO (Fig. 6a). Contrarily, addition of EDTA-2Na or BQ faster represses the rate of RhB photodegradation in the presence of CdS/Ag/Bi_2MoO_6 compared to that in the presence of CdS/Bi_2MoO_6 (Fig. 10). It is noteworthy that the Z-scheme charge transfer pathway not only greatly improves the separation of electron-hole pairs, but also preserves strong and continuous redox ability. According to the above-mentioned discussion, the Z-scheme CdS/Ag/Bi_2MoO_6-catalyzed RhB photodegradation can be proposed as follows:

C/A/BMO+ hν (visible light) →C/A/BMO ($e^- + h^+$) ....(1)

RhB + h^+ → degradation ....(2)

$O_2 + e^- \rightarrow \cdot O_2^-$ ....(3)

RhB + $\cdot O_2^-$→ degradation ....(4)

Conclusions

In summary, a novel Z-scheme photocatalytic system CdS/Ag/Bi_2MoO_6(C/A/BMO) was rationally designed and successfully prepared. As comparison, a series of single-component CdS and Bi_2MoO_6, dual component CdS/Bi_2MoO_6(C/BMO) and Ag/Bi_2MoO_6(A/BMO) were also synthesized. All composites were characterized by XRD, SEM, TEM, XPS, EDX, IR and UV visible spectrum to confirm their phase composite, morphology and structure. The results revealed that Ag and CdS were successfully integrated to the surface of Bi_2MoO_6 to form Ag-Bi_2MoO_6(A/BMO) and CdS-Bi_2MoO_6(C/BMO) as well as CdS-Ag solid-solid contact interfaces in different composite materials Ag/Bi_2MoO_6 (A/ BMO), CdS/Bi_2MoO_6(C//BMO) and CdS/Ag/Bi_2MoO_6(C/A/ BMO), respectively. All materials can be used as photocatlysts for the degradation of RhB dye under visible light irradiations. Owing to the high electronic mobility and strong SPR effect of Ag nanoparticles, the introduction of Ag NPs provides a high-speed charge transfer channel in CdS/Ag/Bi_2MoO_6(C/A/BMO) heterostructure and thereby leads to more efficiently spatial separation of the electrons and holes. Moreover, the photodegradation of RhB dye under visible light irradiation revealed that the multicomposites CdS-Ag-Bi_2MoO_6(C/A/BMO) photocatalytic system exhibited a highest efficient photocatalytic activity compared to the single CdS and Bi_2MoO_6, and dual Ag/Bi_2MoO_6(A/BMO) and CdS/Bi_2MoO_6

View Article Online
DOI: 10.1039/C6NJ01893A

(C/BMO), showing the highly efficient separation of the photogenerated electrons and holes, and stable and strong reducibility and oxidizability in the Z-scheme photocatalytic system CdS-Ag-Bi_2MoO_6(C/A/BMO). Hence a highly efficient photocatalytic performance of CdS-Ag-Bi_2MoO_6(C/A/BMO) can be explained by Z-scheme charge transfer mechanism. Furthermore, the photoluminescence properties and photoelectrochemical properties of single CdS and Bi_2MoO_6, dual Ag/Bi_2MoO_6(A/BMO) and CdS/Bi_2MoO_6(C/BMO) and tri-composite CdS/Ag/Bi_2MoO_6(C/A/BMO) were also investigated in detail, indirectly corroborating the highly photocatalytic performance of Z-scheme catalyst CdS/Ag/Bi_2MoO_6 (C/A/BMO).

Acknowledgements

This work was supported by the National Natural Science Foundation of China (No. 21373159) and the Project of Science & Technology Office of Shaanxi Province (No. 2015SF291, 2013K11-08, 2013SZS20-P01) and Natural Science Program of Education Department of Shaanxi Province (No. 15JS119).

References

1 A. Kubacka, M. Fernandez-Garcia and G. Colon, *Chem. Rev.*, 2012, **112**, 1555–1614.
2 J. Chen, H. B. Yang, J. Miao, H. Y. Wang and B. Liu, *J. Am. Chem. Soc.,* 2014, **136**, 15310–15318.
3 B. Liu, A. Khare and E. S. Aydil, *ACS Appl. Mater. Inter.,* 2011, **3**, 4444–4450.
4 H. Zhang, X. Liu, Y. Li, Q. Sun, Y. Wang, B. J. Wood and H. Zhao, *J. Mater. Chem.,* 2012, **22**, 2465–2472.
5 R. Zhou, Q. Zhang, E. Uchaker, J. Lan, M. Yin and G. Cao, *J. Mater. Chem. A,* 2014, **2**, 2517–2525.
6 L. Yang, C. McCue, Q. Zhang, E. Uchaker, Y. Mai and G. Cao, *Nanoscale,* 2015, **7**, 3173–3180.
7 B. Liu, L. M. Liu, X. F. Lang, H. Y. Wang, X. W. Lou and E. S. Aydil, *Energy Environ. Sci.,* 2014, **7**, 2592–2597.
8 X. B. Chen and S. S. Mao, *Chem. Rev*., 2007, **107**, 2891–2959.
9 B. Frit and J. P. Mercorio, *J. Alloys Compd*.,1992, **188**, 27-35.
10 Y. Shimodaira, H. Kato, H. Kobayashi and A. Kudo, *J. Phys. Chem. B*, 2006, **110**, 17790–17797.
11 H. P. Li, Q. H. Deng, J. Y. Liu, W. G. Hou, N. Du, R. J. Zhang and X. T. Tao, *Catal. Sci. Technol.,* 2014, **4**, 1028–1037.
12 J. C. Jung, H. Kim, A. S. Choi, Y.-M. Chung, T. J. Kim, S. J. Lee, S.-H. Oh and I. K. Song, *Catal. Commun.*, 2007, **8**, 625–628.
13 G. H. Tian, Y. J. Chen, W. Zhou, K. Pan, Y. Z. Dong, C. G. Tian and H. G. Fu, *J. Mater. Chem.*, 2011, **21**, 887–892.
14 D. Yue, D. M. Chen, Z. H. Wang, H. Ding, R. L. Zong and Y. F. Zhu, *Phys.Chem.Chem.Phys.,* 2014, **16**, 26314–26321.
15 L. J. Xie, J. F. Ma and G. J. Xu, *Mater. Chem. Phys*., 2008, **110**, 197–200.
16 W. Z. Yin, W. Z. Wang and S. M. Sun, *Catal. Commun.,* 2010, **11**, 647–650.
17 T. Yan, Q. Yan, X. D. Wang, H. Y. Liu, M. M. Li, S. X. Lu, W. G. Xu and M. Sun, *Dalton Trans.,* 2015,**44**, 1601–1611.
18 J. Tian, P. Hao, N. Wei, H. Z. Cui and H. Liu, *ACS Catal*., 2015, **5**, 4530–4536.
19 Q. Yan, M. Sun, T. Yan, M. M. Li, L. G. Yan, D. Wei and B. Du, *RSC Adv.,* 2015, **5**, 17245–17252.
20 J. W. Fu, S. W. Cao, J. G. Yu, *Journal of Materiomics*, 2015, **1**, 124–133.
21 Y. Zhang, Y. Tang, X. Liu, Z. Dong, H. H. Hng, Z. Chen, T. C. Sum and X. Chen, *Small,* 2013, **9**, 996–1002.
22 X. Wang, C. Liow, D. Qi, B. Zhu, W. R. Leow, H. Wang, C. Xue, X. Chen and S. Li, *Adv. Mater.,* 2014, **26**, 3506–3512.
23 Y. Hu, X. Gao, L. Yu, Y. Wang, J. Ning, S. Xu and X. W. Lou, *Angew. Chem., Int. Ed.,* 2013, **52**, 5636–5639.
24 Q. Li, B. Guo, J. G. Yu, J. R. Ran, B. H. Zhang, H. J. Yan and J. R. Gong, *J. Am. Chem. Soc.,* 2011, **133**, 10878–10884.
25 A. Kudo and Y. Miseki, *Chem. Soc. Rev.,* 2009, **38**, 253–278.
26 M. L. Lu, Z. X. Pei, S. X. Weng, W. H. Feng, Z. B. Fang, Z. Y. Zheng, M. L. Huang and P. Liu, *Phys. Chem. Chem. Phys.,* 2014, **16**, 21280–21288.
27 Y. G. Li, X. L. Wei, H. J. Li, R. R. Wang, J. Feng, H. Yun and A. N. Zhou, *RSC Adv.,* 2015, **5**, 14074–14080.
28 Y. Feng, X. Yan, C. B. Liu, Y. Z. Hong, L. Zhu, M. J. Zhou and W. D. Shi, *Appl. Surf. Sci.,* 2015, **353**, 87–94.
29 P. Zhou, J. G. Yu and M. Jaroniec. *Adv. Mater.,* 2014, **26**, 4920–4935.
30 T. Van Gerven, G. Mul, J. Moulijn and A. Stankiewicz, *Chem. Eng. Process*., 2007, **46**, 781–789.
31 H. Tong, S. Ouyang, Y. Bi, N. Umezawa, M. Oshikiri, J. Ye, *Adv. Mater.*, 2012, **24**, 229–251.
32 Q. J. Xiang, J. G. Yu and M. Jaroniec, *J. Am. Chem. Soc.,* 2012, **134**, 6575–6578.
33 M. G. Kibria, H. P. T. Nguyen, K. Cui, S. Zhao, D. Liu, H. Guo, M. L. Trudeau, S. Paradis, A. R. Hakima and Z. Mi, *ACS Nano*, 2013, **7**, 7886–7893.
34 Q. Zhang, E. Uchaker, S. L. Candelaria and G. Cao, *Chem. Soc. Rev.,* 2013, **42**, 3127–3171.
35 J. A. Christians, R. C. M. Fung and P. V. Kamat, *J. Am. Chem. Soc.,* 2014, **136**, 758–764.
36 S. C. Roy, O. K. Varghese, M. Paulose and C. A. Grimes, *ACS Nano*, 2010, **4**, 1259–1270.
37 A. Dhakshinamoorthy, S. Navalon, A. Corma and H. Garcia, *Energy Environ. Sci.,* 2012, **5**, 9217–9233.
38 E. V. Kondratenko, G. Mul, J. Baltrusaitis, G. O. Larrazábal and J. Pérez-Ramírez, *Energy Environ. Sci.,* 2013, **6**, 3112–3135.
39 J. Kim, J. Lee and W. Choi, *Chem. Commun.,* 2008, 756–758.
40 J. G. Yu and X. X. Yu, *Environ. Sci. Technol.,* 2008, **42**, 4902–4907.
41 Y. Bi, S. Ouyang, N. Umezawa, J. Cao and J. Ye, *J. Am. Chem., Soc.,* 2011, **133**, 6490–6492.
42 X. Li, J. G. Yu, J. X. Low, Y. P. Fang , J. Xiao and X. B. Chen, *J Mater Chem. A*, 2015, **3**, 2485–2534.
43 H. Tada, T. Mitsui, T. Kiyonaga, T. Akita and K. Tanaka, *Nat. Mater.,* 2006, **5**, 782–786.
44 P. Li, Y. Zhou, H. J. Li, Q. F. Xu, X. G. Meng, X. Y. Wang, M. Xiao and Z. G. Zou, *Chem. Commun.,* 2015, **51**, 800–803.
45 H. L. Lin, J. Cao, B. D. Luo, B. Y. Xu and S. F. Chen, *Catal. Commun.,* 2012, **21**, 91–95.
46 Y. M. He, L. H. Zhang, B. T. Teng and M. H. Fan, *Environ. Sci. Technol.,* 2015, **49**, 649–656.
47 Z. H. Cheng, F. Bing, Q. Liu, Z. G. Zhang and X. M. Fang, *J. Mater. Chem. A,* 2015, **3**, 4652–4658.
48 J. Zhang, C. G. Niu, J. Ke, L. F. Zhou and G. M. Zeng, *Catal. Commun.,* 2015, **59**, 30–34.
49 R. Y. Xie, L. P. Zhang, H. Xu, Y. Zhong, X. F. Sui and Z. P. Mao, *J. Mole. Catal. A: Chem.,* 2015, **406**, 194–203.
50 Y. X. Yang, W. Guo, Y. N. Guo, Y. H. Zhao, X. Yuan and Y. H. Guo, *J. Hazard. Mater.,* 2014, **271**, 150–159.
51 J. J. Li, Y. L. Xie, Y. J. Zhong and Y. Hu, *J. Mater. Chem. A,* 2015, **3**, 5474–5481.
52 X. F. Wang , S. F. Li , Y. Q. Ma, H. G. Yu and J. G. Yu, *J. Phys. Chem. C,* 2011, **115**, 14648–14655.

View Article Online
DOI: 10.1039/C6NJ01893A

53 Y. Y. Bu, Z. Y. Chen, C. J. Sun, *Appl. Catal. B: Environ.,* 2015, **179**, 363–371.
54 H. J. Cheng, J. G. Hou, H. M. Zhu and X. M. Guo, *RSC Adv.,* 2014, **4**, 41622–41630.
55 J. G. Hou, C. Yang, Z. Wang, Q. H. Ji, Y. T. Li, G. C. Huang, S. Q. Jiao and H. M. Zhu, *Appl. Catal. B: Environ.,* 2013, **142-143**, 579–589.
56 L. Q. Ye, Ji. Y. Liu, C. Q. Gong, L. H. Tian, T. Y. Peng and L. Zan, *ACS Catal.,* 2012, **2**, 1677–1683.
57 K. P. Xie , Q. Wu, Y. Y. Wang, W. X. Guo, M. Y. Wang, L. Sun and C. J. Lin, *Electrochem. Commun.,* 2011, **13**, 1469–1472.
58 X. W. Wang, G. Liu, L. Z. Wang, Z. G. Chen, G. Q. Lu and H. M. Cheng, *Adv. Energy Mater.,* 2012, **2**, 42–46.
59 M. R. Jones, K. D. Osberg, R. J. Macfarlane, M. R. Langille and C. A. Mirkin, *Chem. Rev.,* 2011, **111** , 3736–3827.
60 W. B. Hou and S. B. Cronin, *Adv. Funct. Mater.,* 2013 , **23** , 1612–1619.
61 H. F. Li, H. T. Yu, X. Quan, S. Chen and Y. B. Zhang, *ACS Appl. Mater. Interfaces*, 2016, **8**, 2111−2119.
62 D. J. Wang, G. L. Xue, Y. Z. Zhen, F. Fu and D. S. Li, *J. Mater. Chem.,* 2012, **22**, 4751–4758.
63 H. Xu, Y. G. Xu, H. M. Li, J. X. Xia, J. Xiong, S. Yin, C. J. Huang and H. L. Wan, *Dalton Trans.,* 2012, **41**, 3387–3394.
64 Y. S. Xu and W. D. Zhang, *Dalton Trans.,* 2013, **42**, 1094–1101.
65 M. Y. Zhang, C. L. Shao, J. B. Mu, X. M. Huang, Z. Y. Zhang, Z. C. Guo, P. Zhang and Y. C. Liu, *J. Mater. Chem.,* 2012, **22**, 577–584.
66 S. Guo, X. F. Li, H. Q. Wang, F. Dong and Z. B. Wu, *J. Colloid Interf. Sci.,* 2012, **369**, 373–380.
67 A. Thomas, A. Fischer, F. Goettmann, M. Antonietti, J. O. Muller, R. Schlogl and J. M. Carlsson, *J. Mater. Chem.,* 2008, **18**, 4893–4908.
68 Z. Fang, Y. F. Liu, Y. T. Fan, Y. H. Ni, X. W. Wei, K. B. Tang, J. M. Shen and Y. Chen, *J. Phys. Chem. C,* 2011, **115**, 13968–13976.
69 R. M. Mohamed and F. M. Ibrahim, *Int. J. Hydrogen Energ.,* 2014, **39**, 14479–14486.
70 H. P. Li, T. X. Hu, R. J. Zhang, J. Q. Liu and W. G. Hou, *Appl. Catal. B: Environ*., 2016, **188**, 313–323.
71 F. Chen, C. G. Niu, Q. Yang, X. M. Li and G. M. Zeng, *Ceram. Int.,* 2016, **42**, 2515–2525.
72 M. Y. Zhang, L. Li, Y. Liu, L. L. Xu and X. T. Zhang, *J. Mol. Catal. A: Chem.*, 2015, **400**, 154–161.
73 L.W. Zhang, T. G. Xua, X. Zhao and Y. F. Zhu, *Appl. Catal. B: Environ.,* 2010, **98**,138–146.
74 J. Fu, B. B. Chang, Y. L. Tian, F. N. Xi and X. P. Dong, *J. Mater. Chem. A,* 2013, 1, 3083–3090.
75 I. Honma, T. Sano, and H. Komiyama, *J. Phys. Chem.,* 1993, **97**, 6692–6695.
76 M. A. Butler, *J. Appl. Phys.,* 1977, **48**, 1914–1920.
77 H. W. Huang, L. Y. Liu, Y. H. Zhang and N. Tian, *J. Alloy Compd.,* 2015, **619**, 807–811.
78 S. Kumar, S. Khanchandani, M. Thirumal and A. K. Ganguli, *ACS Appl. Mater. Inter.,* 2014, **6**, 13221–13233.
79 Y. He, Y. H. Zhang, H. W. Huang, N. Tian and Y. Luo, *Inorg. Chem. Commun.,* 2014, **40**, 55–58.
80 H. W. Huang, G. Chen and Y. H. Zhang, *Chem. Commun.*, 2014, **44**, 46–49.
81 X. F. Hu, T. Mohamood, W. H. Ma, C. C. Chen and J. C. Zhao, *J. Phys. Chem. B,* 2006, **110**, 26012–26018.
82 J. W. Tang, Z. G. Zou and J. H. Ye, *J. Phys. Chem. B,* 2003, **107**, 14265–14269.
83 Z. Dai, F. Qin, H. P. Zhao, J. Ding, Y. L. Liu and R. Chen, *ACS Catal.,* 2016, **6**, 3180−3192.
84 Q. J. Xiang, J. G. Yu and M. Jaroniec, *J. Phys. Chem. C,* 2011, **115**, 7355–7363.
85 T. Yan, M. Sun, H. Y. Liu, T. T. Wu, X. J. Liu, Q. Yan, W. G. Xu and B. Du, *J. Alloy Compd.,* 2015, **634**, 223–231.
86 Z. Hosseini, N. Taghavinia, N. Sharifi, M. Chavoshi and M. Rahman, *J. Phys. Chem. C,* 2008, **112**, 18686–18689.
87 X. J. Bai, L. Wang, R. L. Zong, Y. H. Lv, Y. Q. Sun and Y. F. Zhu, *Langmuir,* 2013, **29**, 3097–3105.
88 Z. Dai, F. Qin, H. P. Zhao, F. Tian, Y. L. Liu and R. Chen, *Nanoscale,* 2015, **7**, 11991-11999.
89 P. Ji, J. Zhang, F. Chen and M. Anpo, *Appl. Catal. B: Environ.,* 2009, **85**, 148–154.
90 M. C. Yin, Z. S. Li, J. H. Kou and Z. G. Zou, *Environ. Sci. Technol.,* 2009, **43**, 8361–8366.
91 J. Jin , J. G Yu, D. P. Guo, C. Cui and W. K. Ho, *Small*, 2015, 11, **39**, 5262–5271.
92 J. Xing, Z. P. Chen, F. Y. Xiao, X. Y. Ma, C. Z. Wen, Z. Li and H. G. Yang, *Chem-Asian. J.,* 2013, **8**, 1265–1270.
93 J. T. Li, S. K. Cushing, J. Bright, F. Meng, T. R. Senty, P. Zheng, A. D. Bristow and N. Q. Wu, *ACS Catal.,* 2013, **3**, 47–51.

View Article Online
DOI: 10.1039/C6NJ01893A

Manuscript for ***New Journal of Chemistry***

Design and Construction of the Sandwich-Like Z-scheme Multicomponent CdS/Ag/Bi_2MoO_6 Heterostructure with Enhanced Photocatalytic Performance in RhB Photodegradation

Danjun Wang,[a] Huidong Shen,[a] Li Guo,[a] Feng Fu*[a] and Yucang Liang*[b]

[a] College of Chemistry &Chemical Engineering, Yan'an University, Shaanxi Key Laboratory of Chemical Reaction Engineering, Yan’an 716000, China

[b] Institut für Anorganische Chemie, Eberhard Karls Universität Tübingen, Auf der Morgenstelle 18, 72076 Tübingen, Germany

Corresponding Author

Dr. Yucang Liang

Institut für Anorganische Chemie, Eberhard Karls Universität Tübingen

Auf der Morgenstelle 18, 72076 Tübingen, Germany

Fax: +49(0)7071 292436

E-mail: yucang.liang@uni-tuebingen.de

Prof. Dr. Feng Fu

College of Chemistry &Chemical Engineering, Yan'an University

Shaanxi Key Laboratory of Chemical Reaction Engineering, Yan’an 716000, China

E-mail: yadxfufeng@126.com

View Article Online
DOI: 10.1039/C6NJ01893A

For table of contents use only:

Design and Construction of the Sandwich-Like Z-scheme Multicomponent CdS/Ag/Bi_2MoO_6 Heterostructure with Enhanced Photocatalytic Performance in RhB Photodegradation

Danjun Wang,[a] Huidong Shen,[a] Li Guo,[a] Feng Fu*[a] and Yucang Liang*[b]

Summary:

A rationally designed and successfully fabricated all-solid-state Z-scheme photocatalyst CdS/Ag/Bi_2MoO_6 with sandwich-like multicomponent heterostructure shows an enhanced photocatalytic performance in RhB photodegradation due to a highly efficient separation of the photogenerated electrons and holes.

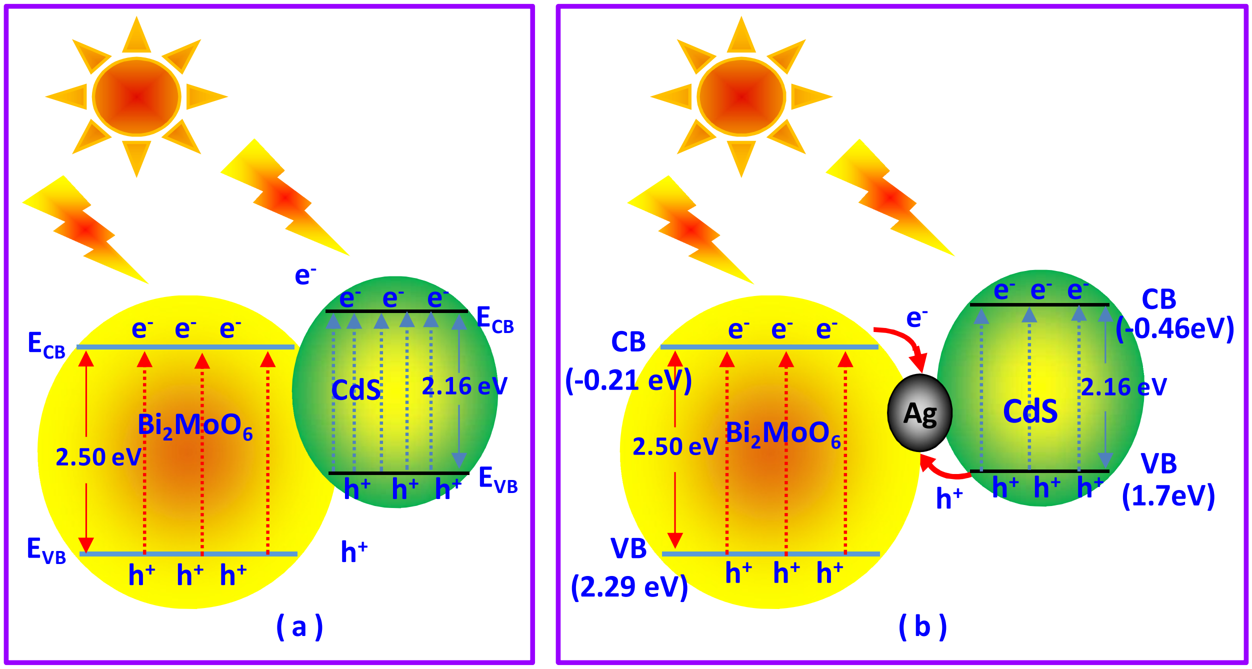

Charge transfer of (a) CdS/Bi_2MoO_6 and (b) CdS/Ag/Bi_2MoO_6 during photocatalytic process